ACS APPLIED MATERIALS & INTERFACES

Research Article

www.acsami.org

Hierarchical Mesoporous MnO_2 Superstructures Synthesized by Soft-Interface Method and Their Catalytic Performances

Yanyu Liu,[†] Zhiwen Chen,*[,†,‡] Chan-Hung Shek,*[,‡] C. M. Lawrence Wu,[‡] and Joseph K. L. Lai[‡]

[†]School of Environmental and Chemical Engineering, Shanghai University, Shanghai 200444, People's Republic of China

[‡]Department of Physics and Materials Science, City University of Hong Kong, Tat Chee Avenue, Kowloon Tong, Hong Kong

ABSTRACT: To obtain a highly efficient and stable heterogeneous catalyst in catalytic wet hydrogen peroxide oxidation, we have successfully synthesized hierarchical mesoporous manganese dioxide (MnO_2) superstructures by a facile and environmental friendly method on a soft-interface between CH_2Cl_2 and H_2O without templates. The main crystal phase of as-prepared MnO_2 was proved to be ε-MnO_2 by X-ray diffraction techniques. The structure characterizations indicated that the hierarchical MnO_2 superstructures were composed of urchin-like MnO_2 hollow submicrospheres assembled by one-dimension nanorods building blocks with rich mesoporosity. The nitrogen sorption analysis confirmed that the as-synthesized MnO_2 has an average pore diameter of 5.87 nm, mesoporous volume of 0.451 $cm^3\ g^{-1}$, and specific surface area of 219.3 $m^2\ g^{-1}$. Further investigations revealed that a possible formation mechanism of this unique hierarchical superstructure depended upon the synthesis conditions. The catalytic performances of the hierarchical mesoporous MnO_2 superstructures were evaluated in catalytic degradation of methylene blue in the presence of H_2O_2 at neutral pH, which demonstrated highly efficient catalytic degradation of the organic pollutant methylene blue using hierarchical mesoporous MnO_2 superstructures as catalyst at room temperature.

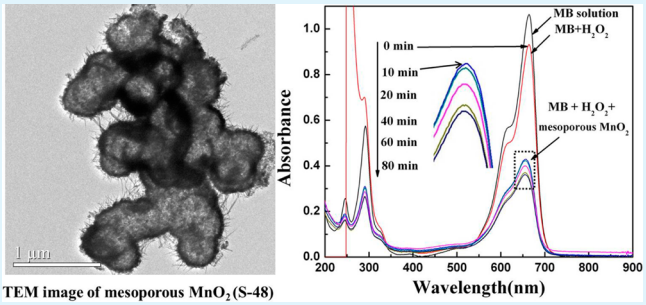

TEM image of mesoporous MnO_2 (S-48)

KEYWORDS: *manganese dioxide, hierarchical mesoporous superstructure, formation mechanism, heterogeneous catalyst, methylene blue*

1. INTRODUCTION

The degradation of refractory organic pollutants has attracted much attention in recent years because they can cause great harm to the natural environment and human health. In particular, the industrial dyes are one of the largest groups of pollutants.[1,2] These dyes usually have complex aromatic molecular structures which make them more stable and more difficult to degrade. If not treated, these hazardous substances will induce certain health hazards and environmental pollution.[3] For example, methylene blue (MB), one of the colored organic compounds, is widely used as a common dye for dying cotton, wood, and silk, a common photosensitizer employed in solar cells, a photodynamic antimicrobial agent in biological materials and a test compound in semiconductor photocatalysis.[4,5] It can result in permanent burns to the eyes of human and animals, nausea, vomiting, profuse sweating, mental confusion, and methemoglobinemia.[6] The widespread of dye industries, which amounts to more than seven million tons annually produced worldwide, combined with the potential carcinogenic risk, causes severe environmental pollution.[7] Therefore, the removal of dyes from industrial effluents has been a major concern in wastewater treatments.

Although traditional treatment techniques, such as physical adsorption,[8,9] chemical oxidation,[10] and biological method,[11] they have been investigated to removal dye from wastewater, many problems are still unavoidable, such as secondary pollution[1] and retarded biodegradation of the accompanying pollutants.[12] Advanced oxidation processes (AOPs), defined as those technologies that utilize the hydroxyl radical (·OH) for oxidation, have received increasing attention in the research of wastewater treatment technologies in the past decades. These processes, such as photocatalytic oxidation, Fenton's chemistry, and ozonation, have been applied successfully for the removal or degradation of recalcitrant pollutants, or used as pretreatment to convert pollutants into shorter-chain compounds that can then be treated by conventional or biological methods.[13] So they have been developed as advanced strategies for the degradation of dyes in aqueous media by the generation of very active species in the presence of catalysts.[14] One of them is the classic Fenton process (dissolved Fe^{2+} and H_2O_2), which is capable of degrading organic pollutants into harmless chemicals, such as CO_2 and H_2O.[4] However, the application of the classical Fenton reagent, i.e., Fe^{2+}/Fe^{3+}-H_2O_2, is limited by the narrow working pH range (2−4) associated with this process[15,16] and by separation and recovery of the iron species specially in industrial wastewater treatment.[17,18] To overcome these drawbacks, some efforts have been made to develop heterogeneous Fenton systems which can be used over a wider

Received: April 11, 2014
Accepted: June 2, 2014
Published: June 2, 2014

   dx.doi.org/10.1021/am502191k | ACS Appl. Mater. Interfaces 2014, 6, 9776−9784

pH range for the degradation of organic pollutants.[19] So far, many heterogeneous Fenton-like catalysts have been reported, such as iron oxides,[20,21] iron oxide nanoparticles supported on mesoporous silica,[19,22] supported on clays,[23,24] combined with carbon materials,[25,26] or iron-containing ZSM-5.[27] In addition to iron oxides, copper oxides,[28] manganese oxides,[1,15] rare earth,[29] and noble metal elements[30] can be also included in the heterogeneous catalysts for the AOPs. In the case of heterogeneous catalysis, there are also some problems, like the lower use efficiency of H_2O_2, the high expense of noble metal, and the dissolution of copper oxides in solution. Therefore, further study is necessary to find out inexpensive, highly efficient and stable heterogeneous catalyst to remove and degrade the organic dyes in catalytic wet hydrogen peroxide oxidation. Obviously, the preparation of highly efficient and stable heterogeneous catalyst has been the key to industrial applications of wet catalytic oxidation.

Since the Fenton reaction involves an electron transfer process, the catalysts with accessible multiple oxidation states should have an excellent catalytic performance.[4] Among transition metal oxides with various oxidation states, manganese oxides as technologically important materials have been widely used as effective catalysts, molecular adsorbent, magnetic materials, electrochemical supercapacitors, and electrode materials for batteries due to their outstanding structural flexibility and physical and chemical properties.[31−35] Among all of manganese oxides, manganese dioxides (MnO_2) have different polymorphs, such as α-MnO_2, β-MnO_2, γ-MnO_2, δ-MnO_2, and ε-MnO_2, which can be applied in the area of catalyst, ion exchange, electrochemical supercapacitor.[4,35] In particular, they can be used as heterogeneous catalyst for catalytic degradation of organic dyes.[33−36] Developing new materials with excellent performance depend not only on the composition but also on their morphology and micro/nanostructures.[35] Various MnO_2 micro/nanostructures, such as nanoparticles, nanorods/belts/wires/tubes/fibers, nanosheets, mesoporous/molecular sieves, branched structures, urchins/orchids, and other hierarchical structures, have been synthesized by different methods.[33] Mesoporous materials as catalysts, catalysts supports, adsorbents, and nanoreactor, have aroused enormous attention because of their high surface area, tunable pore size, adjustable framework, and surface properties.[37,38] From the mesoporous manganese oxide structures reported by previous literatures,[39−42] mesoporous manganese oxides have attracted significant interest because of their unique catalytic, electrochemical, magnetic, and adsorptive properties. In recent years, hierarchically structured mesoporous manganese oxides self-assembled by nanostructures have attracted a concern of materials scientists because of their widespread potential applications in catalysis.[43−45] Controlled self-assembly of micro/nanostructures with hierarchy is a new challenge for new material synthesis and device fabrication.[46,47] Currently, the synthesis of mesoporous MnO_2 with larger specific surface area and proper pore size distribution usually needs extension of the templating procedure,[48−51] such as surfactant as soft template or mesoporous silica as hard template. However, the use of templates is prone to import impurities in the post-treatment to remove the organic species so that it increases the production cost and complexity.[52] Therefore, an easily controlled method without templates to prepare mesoporous MnO_2 structure is more promising than the template methods in industrial manufacturing because of its simplicity and low cost. Recently, an organic-aqueous soft-interface method has been established as an alternative approach to conventional homogeneous synthesis.[52−54]

Herein, we report a simple self-assembly synthesis of urchin-like ε-MnO_2 hollow submicrospheres via a redox reaction involving MnO_4^- and Mn^{2+} on the CH_2Cl_2/H_2O interface, which are composed of mesoporous MnO_2 superstructures with hierarchical porosity and large specific surface area. Further investigations revealed that a possible formation mechanism of this unique hierarchical superstructure depends upon the synthesis conditions. The catalytic performances of the hierarchical mesoporous MnO_2 superstructures were evaluated in the catalytic degradation of methylene blue in the presence of H_2O_2 at room temperature.

2. EXPERIMENTAL SECTION

Sample Synthesis. The method of preparing mesoporous MnO_2 in this study is from improvement of the previous works.[44,52] $MnSO_4$, $KMnO_4$, and CH_2Cl_2 were purchased from the Sino pharm Chemical Reagent Co. Ltd. (Shanghai, China). All chemicals used in this study were of analytical grade without further purification. All aqueous solutions were freshly prepared using high-purity water. First, 30 mL of 1 M $MnSO_4$ solution was added into 80 mL of dichloromethane in a beaker of 200 mL. After 5 min, the obvious H_2O/CH_2Cl_2 interface was obtained. Then 80 mL of 0.25 M $KMnO_4$ solution, through the CH_2Cl_2 layer by 30 drops/min controlled by a faucet of dropping funnel, reached the CH_2Cl_2/H_2O interface along the tube of the funnel. During the reaction process, a brown material appeared at the interface and the $MnSO_4$ solution layer slowly turns to brown. After 48 h, the brown products were collected by the vacuum pumping filtration equipment, washed for 3 times with high-purity water and for 1 time with absolute ethanol, and finally dried at 80 °C in the air for 12 h. The collected sample was denoted as S-48. To investigate the formation mechanism of MnO_2 hollow microspheres, some comparative experiments in which the brown samples had collected at 12 and 24 h were carried out with keeping the other experimental conditions unchanged. These collected samples were denoted as S-12 and S-24, respectively. In order to improve the catalytic capacity of S-48, the S-48 sample was calcined in a muffle furnace in air from room temperature to 300 °C with a ramp rate of 5 °C/min and kept at this temperature for 2 h. This calcined sample was named S-48−300 °C.

Materials Characterization. All samples prepared in "Sample Synthesis" section have not undergone further thermal treatment before various materials characterizations. The samples were examined by powder X-ray diffraction (XRD) (18KW D/MAX2500 V+/PC, Japan) using a CuK_α source (λ = 0.1542 nm). Scanning electron microscopy (SEM) images were taken with a field-emission scanning electron microscope (FESEM) at 15 kV (JSM-6700F, Japan). Micro/nanostructures of the samples were observed with transmission electron microscope (TEM, JEM-2010F, Japan). Surface area and porosity of the samples were determined by Brunauer−Emmett−Teller (BET) measurements on N_2 adsorption/desorption at 77 K with a Quantachrome Surface Area Analyzer (QUDRASORB SI, USA).

Catalytic Performances. The measurement method of catalytic activity in this study was based on the reports by Yang et al.[2,55] The catalytic performances of the obtained mesoporous MnO_2 superstructures were evaluated in the catalytic oxidation of methylene blue (MB). In order to obtain the exact weight of catalyst, the 110 °C was selected as the thermal treatment temperature due to the moisture in the long-laid samples. The catalyst to be tested was dried at 110 °C for 10 h. First, 50 mL of the MB dye solution (100 mg/L) and 10 mL of the H_2O_2 solution (30 wt %) were combined in a 250 mL glass flask, then 25 mg of the no-moisture MnO_2 catalysts was added into the flask. The catalytic reaction was carried out in a shaking incubator (constant temperature at 30 °C, 100 r/min, and atmospheric pressure). For a given time interval, 1 mL of the mixture solution was pipetted into a centrifuge tube with 0.25 mL of tert-butanol and quickly diluted with distilled water to 20 mL. The diluted solution was

immediately centrifuged (rotating speed at 1000 r/min for 10 min) in order to remove the catalyst particles, which tend to scatter the incident beam. The filtered dye solution was then put into a quartz cell (path length 1.0 cm) and the absorption spectrum was measured with a double-beam ultraviolet−visible (UV−vis) spectrophotometer (TU-1901, Beijing Puxi Universal Apparatus Co. Ltd., China). A linear calibration curve for the dye concentrations was obtained by monitoring the peak intensity at λ_{max} = 664 nm for a series of standard solutions according to the Beer's law. Degradation rate of the MB in 60 min as a function of reused times of the catalyst and the dissolubility of the catalyst in mixed solution were selected as indexes to assess the catalytic stability of the catalysts. The concentration of Mn ion in the solution was determined by an inductive coupled plasma emission spectrometer (ICP, 2A051657, LEEMAN LABORATORIES INC, USA).

3. RESULTS AND DISCUSSION

The S-12, S-24, and S-48 samples were obtained at different reaction time of 12, 24, and 48 h, respectively. The crystal phases of the as-prepared MnO_2 three samples were characterized by powder XRD. Figure 1 shows the wide-angle

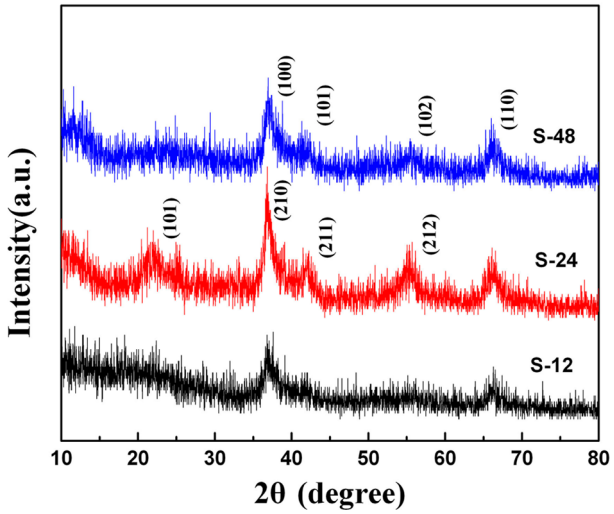

Figure 1. XRD patterns of the as-synthesized MnO_2 three samples: S-12, S-24, and S-48.

XRD patterns of the as-synthesized MnO_2 three samples. As seen from the wide-angle pattern of the S-12 sample, only three weaker diffraction peaks at 2θ = 36.8, 37.0, and 66.3° are near to the characteristic peaks of MnO_2 as shown in Table 1,

Table 1. Four Characteristic Peaks of XRD Patterns in γ-MnO_2 and ε-MnO_2

crystal phases	location of characteristic peaks (deg)			
γ-MnO_2	22.0	36.9	55.8	56.8
ε-MnO_2	37.1	42.4	56.0	66.8

indicating that the S-12 is in the early stage of forming MnO_2. For the S-24 sample, there are obvious diffraction peaks at 2θ = 22.0, 36.8, 42.2, 55.7, and 66.1° in the XRD patterns. The peaks at 2θ = 22.0, 36.8, and 55.7° can be easily identified for the (101), (210), and (212) planes of the γ-MnO_2 crystalline structure (Ramsdellite, syn MnO_2, JCPDS file No.: 44−0142). While the peaks at 2θ = 42.2, and 66.1° can be indexed to ε-MnO_2 (Akhtenskite, syn MnO_2, JCPDS file No.: 30−0820). The XRD results indicate that the S-24 sample is a mixture of γ-MnO_2 and ε-MnO_2. Compared with the S-24 sample, the peaks at 2θ = 22.0, and 55.7° have weakened or disappeared obviously in the XRD pattern of S-48. For the S-48 sample, the peaks at 2θ = 37.0, 42.0, 55.6, and 66.9° are more aligned with that of pure ε-MnO_2. Above XRD results demonstrate that the transformation of crystalline structure during the aging process: γ-MnO_2 turns to ε-MnO_2. The crystal phase of the as-prepared MnO_2 three samples in this study is different to the previous reports by Yuan and co-workers,[44,52] which is attributed to the differences of reagent and soft interface. All diffraction peaks of the MnO_2 three samples are broad and weak because of the poor crystallinity or the small crystal domain in the products, which results from the low preparation temperature.[32]

The morphologies of the obtained MnO_2 three samples were examined by SEM, TEM, and Brunauer−Emmett−Teller (BET) measurements on N_2 adsorption/desorption at 77 K. Figure 2 shows the field-emission SEM (FESEM) images of the

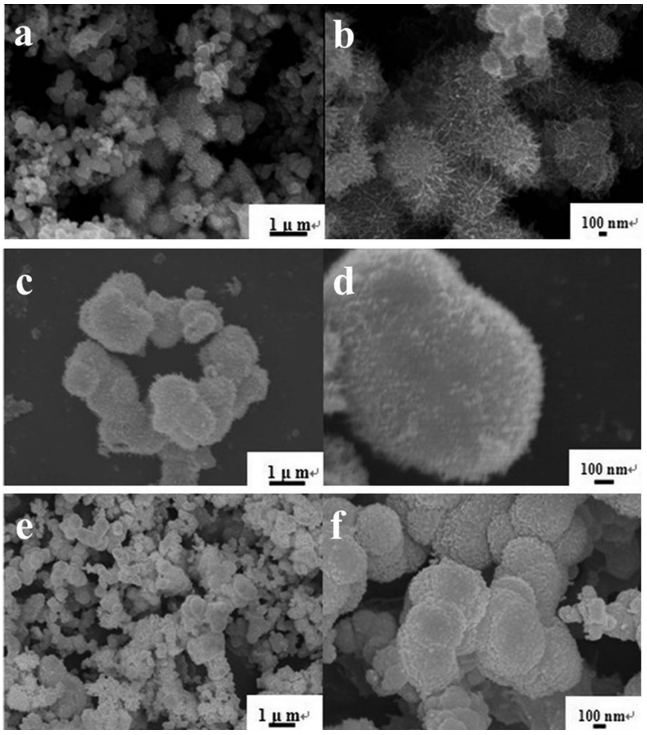

Figure 2. FESEM images at different magnifications of the MnO_2 three samples: (a, b) S-12, (c, d) S-24, and (e, f) S-48.

as-synthesized MnO_2 three samples. As seen from the lower-magnification FESEM image of the S-12 sample as shown in Figure 2a, the panoramic morphology is composed of numerous submicrospheres with thorns on the surface. The higher-magnification FESEM image of the S-12 sample as shown in Figure 2b reveal that the surface of the urchin-like spheres seems to have numerous nanorods, which implies that the nanorods build automatically up the submicrospheres. Compared to Figure 2a, b, the FESEM images of the S-24 (Figure 2c, d) and S-48 (Figure 2e, f) samples at different magnifications indicate that the submicrospheres are larger, dense, and smooth than those of the S-12 sample, and the nanorods on the surface of urchin-like spheres become compact and unobvious, which suggests that the morphologies of submicrospheres in the S-24 and S-48 samples have been

improved in the growing stage because of increasing reaction time, such as 24 and 48 h.

The morphologies and micro/nanostructures of the MnO_2 urchin-like spheres were further examined by TEM imaging. Figure 3 shows the TEM images of the S-12 (Figure 3a, b), S-24 (Figure 3c, d) and S-48 (Figure 3e, f) at different magnifications. It can be seen that the three samples predominantly consist of the hollow urchin structure with visible interior cavities as shown in Figure 3a, c, e. A few spheres with surface damage as shown in Figure 3e are also observed, further suggesting that the as-synthesized MnO_2 submicrospheres have the hollow structures. Nanomeasurer software was used to analyze SEM and TEM images, which present that the S-12 sample has the submicrospheres with size ranges from 150 to 300 nm, whereas the submicrospheres of the S-24 and S-48 samples are confined to the size range of 200−400 nm and 200−500 nm, respectively. In a contrast to the microspheres prepared by Yuan et al.[44,52] and Chen et al.,[34] the as-synthesized submicrospheres in this study have smaller diameter, which may be ascribed to the different thickness of soft-interface. The TEM images easily demonstrate the fact that the average diameter (~400 nm) of MnO_2 submicrospheres in the S-48 sample is larger than that (~213 nm) of the S-12 and that (~362 nm) of the S-24, which indicates that the MnO_2 submicrospheres are growing in the aging progress. This verdict can be also supported by the higher-magnification TEM images of the S-12, S-24, and S-48 three samples as shown in Figure 3b, d, and f, respectively. The higher-magnification TEM images offer an obvious view of the surface microstructure, which exhibits that the urchin-like hierarchical MnO_2 submicrospheres are composed of numerous compactly nanorods growing in all directions. This further reveals that the as-prepared MnO_2 submicrospheres are assembled from lots of one-dimension MnO_2 nanorods building blocks with rich mesoporosity. The careful consideration on the higher-magnification TEM image as shown in Figure 3f would tell us the mesopores also exist in the gaps between submicrospheres.

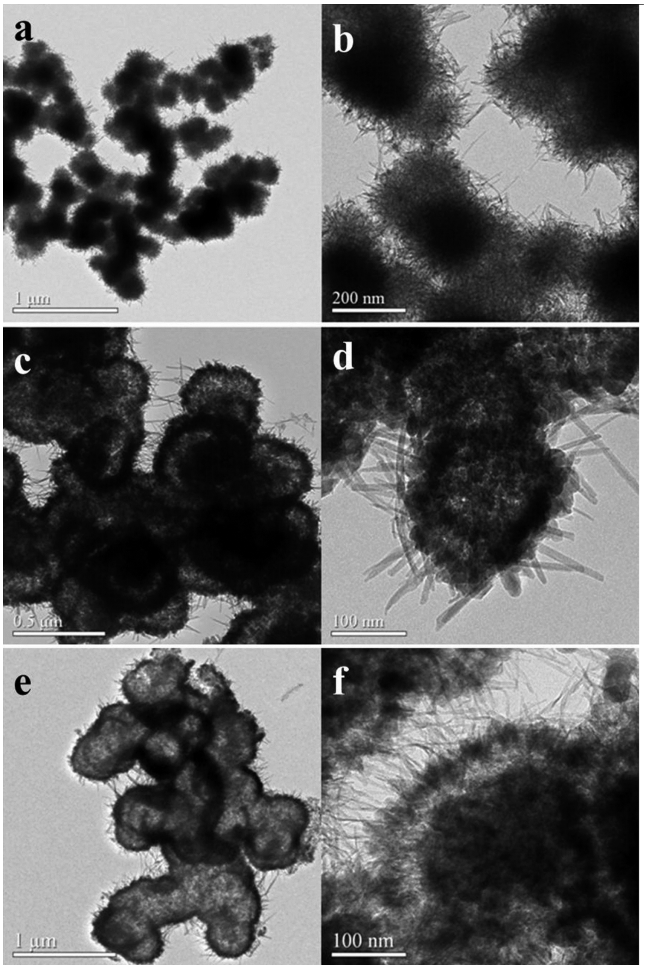

Figure 3. TEM images at different magnifications of the MnO_2 three samples: (a, b) S-12, (c, d) S-24, and (e, f) S-48.

To further analyze and quantify the specific porous properties of the urchin-like hierarchical MnO_2 superstructures, we carried out the nitrogen adsorption−desorption measurements at 77 K. Because of the little difference of the nitrogen adsorption−desorption isotherms in the S-12, S-24, and S-48 three samples, the pore-size distributions would produce serious mutual interference when their graphs stacked together, which is not conducive to analyze the distinction in the porous properties. So only the contrast of the S-12 and S-48 has been investigated. Figure 4 shows the nitrogen adsorption−desorption isotherms (Figure 4a) and corresponding pore-size distributions (Figure 4b) of the S-12 and S-48 samples. As the N_2 adsorption−desorption isotherms as shown in Figure 4a, they can be classified as type IV according to the international

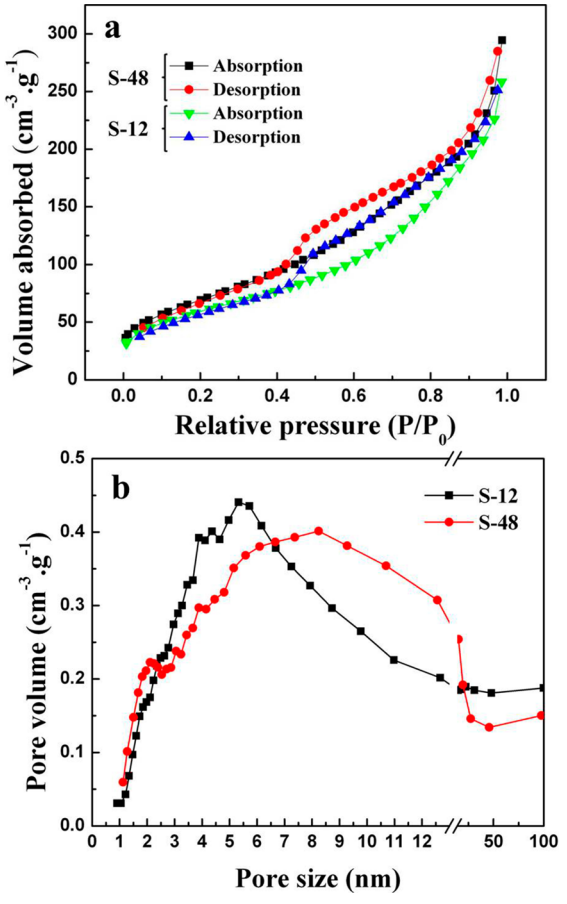

Figure 4. (a) N_2 adsorption−desorption isotherms and (b) corresponding pore-size distributions of the S-12 and S-48 samples, respectively.

dx.doi.org/10.1021/am502191k | ACS Appl. Mater. Interfaces 2014, 6, 9776−9784

union of pure and applied chemistry classification. A distinct type H3 hysteresis loop can be observed in the larger range of 0.4−1.0 P/P_0, providing another evidence for the mesoporous structure of the S-12 and S-48 samples. The measured Brunauer−Emmett−Teller (BET) surface areas of the S-12 and S-48 samples were 254.8 and 219.3 $m^2\ g^{-1}$, respectively, which suggests that specific surface area decreases along with the growth of MnO_2 submicrospheres. The type H3 hysteresis loop demonstrates that the samples consist of particles or split-shape materials, which implies that the as-prepared MnO_2 superstructures should possess hierarchical porosity. This deduction can be further supported by the pore-size distributions of the S-12 and S-48 samples as shown in Figure 4b. The pore sizes of the S-48 sample are distributed in the range 1.3−100 nm, with the majority clustering in the range 1.3−15 nm. The smaller diameter ones are in the range 1.5−2.5 nm and larger diameter ones are in the range 5−10 nm. The hierarchical porosity should be ascribed to mesopores between submicrospherical superstructures and the mesopores existing in the one-dimension MnO_2 nanorods building blocks. Using Barrett−Joyner−Halenda (BJH) method to calculate the average pore diameter from the adsorption branch of the isotherm, the measured average pore diameters of the S-12 and S-48 samples were 3.88 and 1.82 nm, respectively. However, the average pore diameter (5.61 nm) of the S-12 sample was smaller than that (5.87 nm) of the S-48 sample. The seemingly contradictory results support the viewpoint that the nanorods arrange more closely and the gap mesopores become larger owing to the growth of submicrospheres in the aging stage. Moreover, the mesoporous volumes of the S-12 and S-48 samples are quantitatively determined to be 0.471 and 0.451 $cm^3\ g^{-1}$ as shown in Table 2, which further verify the above views. It is interesting that the pores in urchin-like hierarchical MnO_2 submicrospherical superstructures were smaller and more uniform than those of the hierarchical mesoporous materials in previous reports.[34,44,48]

Table 2. Textural Properties of the MnO_2 Three Samples: S-12, S-24, and S-48

	BET area ($m^2 \cdot g^{-1}$)	pore volume ($cm^{-3}\ g^{-1}$)	average pore diameter (nm)
S-12	254.8	0.471	5.61
S-24	228.4	0.459	5.75
S-48	219.3	0.451	5.87

As relevant reports have stated, the interfaces between immiscible fluids have been shown to be ideal for the assembly of nanometer-sized colloidal particles,[53] the particles are highly mobile, and rapidly achieve an equilibrium assembly at a liquid/liquid soft-interface.[54] Yuan and co-workers have given a general explanation for the formation of mesoporous MnO_2 on the H_2O/CCl_4 interface. Obviously, the dynamical soft-interface was formed in the immiscible H_2O/CH_2Cl_2 system. Owing to the different surface tensions, a unique convex occurred on the H_2O/CH_2Cl_2 interface. We would like to propose a possible self-assembly mechanism, such as equilibrium assembly mechanism, to explain the formation of this urchin-like hierarchical MnO_2 submicrospherical superstructure according to the above experimental results. This mechanism is described as follows: when the $KMnO_4$ solution was dropped enter into the $MnSO_4$ solution through the CH_2Cl_2 layer, the redox reaction occurred: $3Mn^{2+} + 2MnO_4^- + 2H_2O = 5MnO_2 + 4H^+$. The theoretical yield of MnO_2 is 4.35 g but the actual output is 4.18 g. So the productive rate is 96%, which verifies the formation of MnO_2 in the acidic reaction. The MnO_2 particles produced in the reaction processes could gradually change into the nanorods, which fell to the H_2O/CH_2Cl_2 interfaces. Because the solubility of MnO_2 in H_2O and CH_2Cl_2 is both very tiny, MnO_2 nanorods distribute along the unique convex interface. In order to minimize the surface energy, these nanorods accumulated at the convex interface start to wrap the lower liquid to form hollow spheres with many mesopores. Thus, the hollow spheres with thorns occurred, many nanorods further aggregated to the surface of the spheres and were dispersed by dynamical mixed liquid to form much bigger submicrospheres. However, the submicrospheres would stop increasing, even happen to burst when submicrosphere diameter increased to a certain degree, which may be related to the thickness of the interface. The thickness of interface mainly results from the concentration difference of the two immiscible fluids. The smaller the difference value is, the thinner the soft interface is larger. So H_2O/CH_2Cl_2 interface is thicker than H_2O/CCl_4 interface. For MnO_2 submicrospheres packing the mixed liquid need to keep the balance of internal and external pressure, MnO_2 submicrospheres would be restricted in the interface layer. As a result, the diameter of MnO_2 submicrospheres is less than the thickness of the interface. For the average density of MnO_2 submicrosphere packing, the mixed liquid is between the densities of H_2O and CH_2Cl_2, so the MnO_2 submicrospheres always kept suspension in the H_2O/CH_2Cl_2 interface environment. The incompact urchin-like MnO_2 submicrospheres have to form numerous mesoporous gaps among them so that the hierarchical MnO_2 submicrospherical superstructures possessed the gap mesopores between submicrospheres and mesopores existing in the one-dimension MnO_2 nanorods building blocks. Therefore, the formation of this urchin-like hierarchical MnO_2 submicrospherical superstructure is mainly ascribed to the significant contribution of the H_2O/CH_2Cl_2 interfaces. This will provide a beneficial reference for further study about the formation of hierarchical superstructures.

The obtained urchin-like hierarchical MnO_2 submicrospherical superstructures (S-48) would be expected to show superior surface-related properties because of tremendous specific surface area, for example, catalytic properties. Herein, the S-48 will be used as a catalyst for wastewater treatment. Methylene blue (MB), as a typical industrial pollutant, was chosen as a model to examine the catalytic performance of this mesoporous MnO_2. The oxidative degradation of the MB dye was investigated under the neutral condition using H_2O_2 as oxidant and the S-48 as catalyst. The UV−vis absorption spectra of the MB solution and mixed solutions added by hydrogen peroxide and S-48 (such as MB + H_2O_2, MB + H_2O_2 + S-48) as a function of the reaction time were shown in the bottom of Figure 5 with chemical structure of MB molecular as shown in the top of Figure 5. The spectrum of the initial solution of MB (no H_2O_2) shows four absorption peaks located at 246, 292, 614, and 664 nm, which originates from the molecular absorption of the MB.[2,32,34] The MB bands at 292 and 246 nm were covered by the strong absorption of hydrogen peroxide in the range of 185−300 nm[2,43] after the MB solution and H_2O_2 solution were mixed. As the S-48 was added, the intensities of the peaks at 614 and 664 nm decreased rapidly within 10 min. As the reaction proceeded, the characteristic absorption of the MB at 664 nm gradually weakens, which is

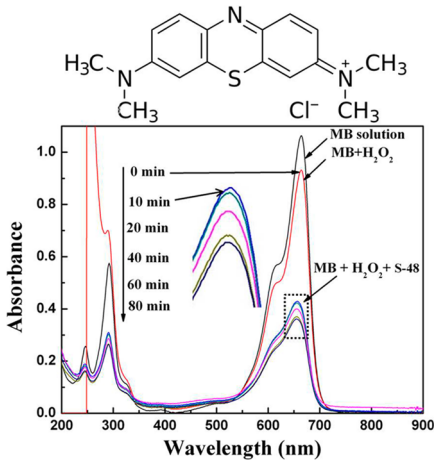

Figure 5. Top: Chemical structure of the MB molecule. Bottom: UV–vis absorption spectra of the MB solution and the mixtures such as MB + H_2O_2, MB + H_2O_2 + mesoporous MnO_2 (S-48) as a function of the reaction time.

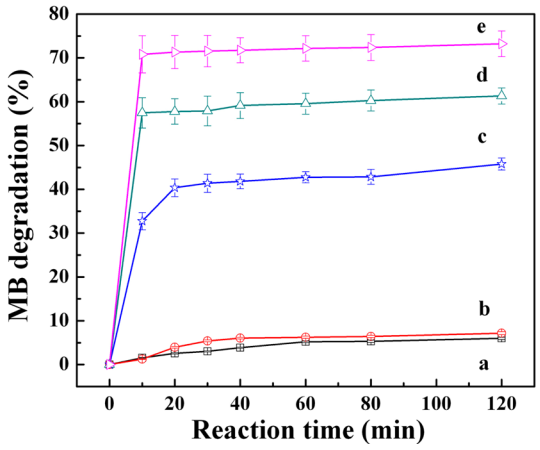

Figure 6. Degradation rate of the MB using H_2O_2 as oxidant and different catalysts: (a) no H_2O_2, (b) no catalyst, (c) commercial MnO_2, (d) the as-prepared mesoporous MnO_2 (S-48), (e) the calcined mesoporous MnO_2 (S-48–300 °C).

why it was chosen for monitoring the catalytic process of the mesoporous MnO_2 superstructures. At the same time, the color of the mixture became shallow gradually. With the further elapse of reaction time after 60 min, the drop of the MB peaks continued but much more slowly. The original absorption maximum at 664 nm shifted to 657 nm after reaction for 10 min. The blue shift of the absorption band indicates that the catalytic degradation of the MB is similar to that reported by Zhang et al.[4] Moreover, the band at 614 nm became very broad and weak at 60 min.

In general, the degradation efficiency of the MB molecules denoted as r in this study was calculated as follows:

$$r = \frac{C_0 - C}{C_0} = \frac{I_0 - I}{I_0} \text{(when dilution multiple is the same)}$$

where C_0 (g L^{-1}) is the initial concentration of the mixture of the MB solution and H_2O_2 solution, C (g L^{-1}) is the concentration of the mixture solution at different intervals during the reaction, I_0 is the absorbance at 664 nm at t = 0 min and I is the absorbance at the same wavelength at a given reaction time. Some reports selected the corresponding absorbance of the MB solution as I_0, neglecting the volume change of the solution when H_2O_2 solution was added. Thus, the degradation ratio has got a bigger value. To get more exact data, the mixture solution of 50 mL of MB and 10 mL of H_2O is selected as the initial solution at t = 0 min in this study. The results about degradation extent are shown in Figure 6. Line a in Figure 6 indicates that the mesoporous MnO_2 (S-48) barely adsorbs MB from the resolution, in agreement with previous results reported in the literatures.[2,15,32] As line b in Figure 6 demonstrates that only ~7.2% of MB is decomposed without catalyst even after reacting for 120 min. No obvious decolorization is observed without H_2O_2 or S-48eVen after 2 h (Figure 6, line a and b), which declares that the degradation of MB molecules is caused by H_2O_2-induced oxidation catalyzed by MnO_2. It can be seen that the ~42.7% of MB can be decomposed in 120 min using the commercial MnO_2 (its specific surface area is 0.2 m^2/g) as catalyst (Figure 6, line c). The similar catalytic performance of commercial MnO_2 has been reported by Zhang et al.[2] The ~57.8% of MB in the solution is decomposed within 20 min in the presence of S-48 as catalyst and ~61.3% of the MB is decomposed after the decomposition reaction was conducted for 120 min (Figure 6, line d), which manifests the catalytic reaction occurred rapidly. Obviously, the catalytic activity of the S-48 is much higher and faster than that of the commercial MnO_2.

The catalytic performance was described only by the conversion degree of MB is unconvincing and improper because the catalytic capacity of the catalyst and the volume of 30 wt % H_2O_2 solution consumed were both responsible for the conversion degree of MB. Since the H_2O_2 was always totally consumed in the catalytic reaction, the catalytic performance of mesoporous MnO_2 could be estimated by the equation as follows

$$q = \frac{(C_0 - C)V_0}{VW} = \frac{M_0 r}{VW}$$

where q (g L^{-1} g^{-1}) is the consumption of MB caused by 1 g of catalyst and 1 L of 30 wt % H_2O_2 solution, C_0 (g L^{-1}) has the same meaning as above but C (g L^{-1}) is the concentration of the mixture solution at 120 min. V_0 (L) is the initial volume of the mixture, i.e., 60 mL, V (L) is the volume of 30 wt % H_2O_2 solution added into MB solution, i.e., 10 mL, W (g) is the weight of the catalyst, i.e., 0.025 g, and M_0 (g) means the initial mass of MB. The q in this study is about 12.26 g L^{-1} g^{-1}, which is more effective than ~2.46 and 8.13 g L^{-1} g^{-1} of β-MnO_2 nanorods (its surface area is 63.8 m^2 g^{-1}),[2,55] ~3.20 g L^{-1} g^{-1} of β-MnO_2 hollow octahedral[43] and ~6.67 g L^{-1} g^{-1} of MnO_2 nanofiber (its surface area is 104 m^2 g^{-1}).[1] The excellent catalytic performance of the urchin-like hierarchical MnO_2 submicrospherical superstructures (S-48) may be due to mesopores between hollow submicrospheres (high surface area) and mesopores existing in the one-dimension MnO_2 nanorods building blocks (high surface-to-volume ratio). The catalytic performance of the as-prepared hierarchical MnO_2 superstructures may be related to their large surface areas.

To further improve the catalytic efficiency of the as-prepared mesoporous MnO_2 superstructures, the S-48 sample has been treated by the calcination of 300 °C for 2 h. Further experiments reveal that the calcined S-48 sample (S-48–300 °C) exhibits higher catalytic performance (in same weight, e.g., 25 mg) than that of S-48 with the increase of 10% in the degradation of MB (Figure 6, line e). Figure 7 shows the XRD

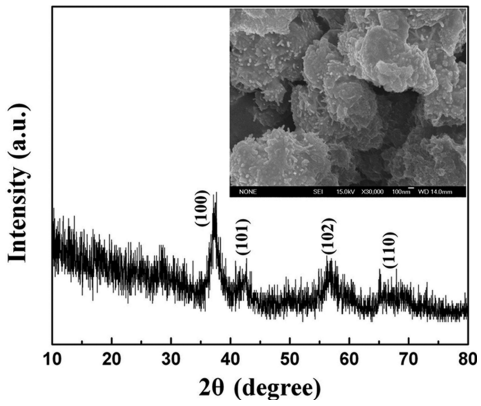

Figure 7. XRD pattern and SEM image (inset) of S-48−300 °C.

pattern and SEM image (inset) of S-48−300 °C. The XRD patterns of the calcined S-48 sample indicate that its crystal phase is also ε-MnO_2 with the improvement of crystallinity. The SEM image (inset) shows the lessened nanorods on the surface of MnO_2 hollow submicrospheres than that of the S-48 sample. Undoubtedly, the surface area of the calcined sample has been decreased after calcination. The higher efficiency of the calcined sample was achieved, which may be ascribed to better crystallinity[21] and cleaner surface[35] of the catalyst. Different morphology of the crystals results in different exposed crystallographic facets that showed different adsorption ability to the reacting agent and then different catalytic activity. The reacting agent is absorbed easier on the clean surface of catalysts before the catalytic reaction. However, further investigations on the promotion of the catalytic performance by the calcination are necessary.

The stability of catalyst is crucial to its application during the catalytic process. Figure 8 shows the degradation of the MB in

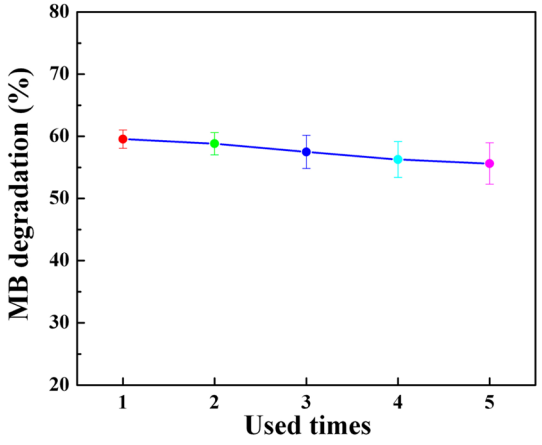

Figure 8. Degradation of the MB in 60 min as a function of reused time using the mesoporous MnO_2 (S-48) as the catalyst.

60 min as a function of reused times using the mesoporous MnO_2 (S-48) as the catalyst. The experiments indicate the slight decrease of catalytic capacity of the hierarchical mesoporous MnO_2 superstructures along with the increase of the used times, which may result from the loss of catalyst and adsorption of organic reactants on the catalyst. The ∼55.6% of the MB was decomposed with the catalyst used in fifth times only with the drop of 4% in comparison to the first time, indicating that the as-prepared mesoporous hierarchical MnO_2 superstructures show superior catalytic stability during the Fenton-like reaction. The dissolubility of the catalyst in solution is also selected as an index to assess the catalytic stability of the catalyst. The concentration of Mn ion in mixed solution detected by inductively coupled plasma-atomic emission spectrometry is 11.3 mg/L, which is in coincidence with the tiny degradation of the MB (∼1.2%) with the filtered solution as catalyst. The two results also indicate that the catalytic wet peroxide oxidation of MB using mesoporous MnO_2 as catalyst is in heterogeneous catalytic system. To conclude, the excellent catalytic performance of the hierarchical MnO_2 superstructures favors their practical applications.

4. CONCLUSIONS

In summary, a soft-interface between CH_2Cl_2 and H_2O as a facile approach has been used to successfully prepare the hierarchical mesoporous MnO_2 superstructures without templates. The superstructures consist of the hierarchical urchin-like MnO_2 hollow submicrospheres with size ranges from 200 to 500 nm. The main crystal phase of as-prepared mesoporous MnO_2 was proved to be ε-MnO_2. This mesoporous MnO_2 has an average pore diameter to be 5.87 nm, mesoporous volume to be 0.451 $cm^3 \cdot g^{-1}$, and specific surface area to be 219.3 $m^2\ g^{-1}$. The formation mechanism of this hierarchical urchin-like MnO_2 superstructure was investigated reasonably, which is based on the self-assembly of one-dimension MnO_2 nanorods, and replied on the synthesis conditions such as the type of interface and aging time. This unique pathway may be applicable to the preparation of other transition metal oxide superstructures for its simplicity and feasible control. Methylene blue, a common dye, was used as model substrate to evaluate the catalytic activity of the as-prepared mesoporous MnO_2. This catalyst exhibits excellent performance for the degradation of methylene blue in the presence of H_2O_2 at neutral pH. This mesoporous MnO_2 superstructure as heterogeneous catalyst can be recycled with tiny decrease of catalytic activity and be stable with its tiny dissolubility in solution. Further experiments reveal that the calcined sample (e.g., 300 °C for 2 h) is able to improve the catalytic performance of as-prepared mesoporous MnO_2. This study demonstrates that the hierarchical mesoporous MnO_2 superstructures have highly efficient catalytic degradation for the organic pollutant methylene blue at room temperature.

AUTHOR INFORMATION

Corresponding Authors

*Phone: +86 21 66137503. Fax: +86 21 66137787. E-mail: zwchen@shu.edu.cn.

*E-mail: apchshek@cityu.edu.hk.

Notes

The authors declare no competing financial interest.

ACKNOWLEDGMENTS

The work described in this article was financially supported by the National Natural Science Foundation of China (Projects 11375111 and 11074161), the Research Fund for the Doctoral Program of Higher Education of China (Projects 20133108110021), the Key Innovation Fund of Shanghai Municipal Education Commission (Projects 14ZZ098 and 10ZZ64), the Science and Technology Commission of Shanghai Municipality (Project Number: 10JC1405400), the Shanghai Pujiang Program (Project Number: 10PJ1404100),

and the Program for Innovative Research Team in University (Project Number: IRT13078). This work was also supported by a General Research Fund from the Research Grants Council, Hong Kong (Project Number: CityU 119212).

REFERENCES

(1) Peng, X. S.; Ichinose, I. Manganese Oxyhydroxide and Oxide Nanofibers for High Efficiency Degradation of Organic Pollutants. *Nanotechnology* **2011**, *22*, 015701.
(2) Zhang, W. X.; Yang, Z. H.; Wang, X.; Zhang, Y. C.; Wen, X. G.; Yang, S. H. Large-Scale Synthesis of Beta-MnO_2 Nanorods and Their Rapid and Efficient Catalytic Oxidation of Methylene Blue Dye. *Catal. Commun.* **2006**, *7*, 408−412.
(3) Zhang, L.; Zhou, X. Y.; Guo, X. J.; Song, X. Y.; Liu, X. Y. Investigation on The Degradation of Acid Fuchsin Induced Oxidation by $MgFe_2O_4$ Under Microwave Irradiation. *J. Mol. Catal. A: Chem.* **2011**, *335*, 31−37.
(4) Zhang, L. L.; Nie, Y. L.; Hu, C.; Hu, X. X. Decolorization of Methylene Blue in Layered Manganese Oxide Suspension with H_2O_2. *J. Hazard. Mater.* **2011**, *190*, 780−785.
(5) Kuan, W. H.; Chen, C. Y.; Hu, C. Y.; Tzou, Y. M. Kinetic Modeling for Microwave-Enhanced Degradation of Methylene Blue Using Manganese Oxide. *Int. J. Photoenergy* **2013**, 916849.
(6) Rafatullah, M.; Sulaiman, O.; Hashim, R.; Ahmad, A. Adsorption of Methylene Blue on Low-Cost Adsorbents: A Review. *J. Hazard. Mater.* **2010**, *177*, 70−80.
(7) Kannan, R.; Peera, S. G.; Obadiah, A.; Vasanthkumar, S. MnO_2 Aupported POM-A Novel Nanocomposite for Dye Degradation. *Dig. J. Nanomater. Bios.* **2011**, *6*, 829−835.
(8) Gupta, V. K.; Suhas. Application of Low-Cost Adsorbents for Dye Removal-A Review. *J. Environ. Manage.* **2009**, *90*, 2313−2342.
(9) Adak, A.; Bandyopadhyay, M.; Pal, A. Removal of Crystal Violet Dye from Wastewater by Surfactant-Modified Alumina. *Sep. Purif. Technol.* **2005**, *44*, 139−144.
(10) Slokar, Y. M.; Majcen Le Marechal, A. Methods of Decoloration of Textile Wastewaters. *Dyes Pigm.* **1998**, *37*, 335−356.
(11) Manal, M. A.; El-Naggar, S.; El-Aasar, A.; Khlood, I. B. Bioremediation of Crystal Violet Using Air Bubble Bioreactor Packed With Pseudomonas Aeruginosa. *Water Res.* **2005**, *39*, 5045−5054.
(12) Chen, C. C.; Liao, H. J.; Cheng, C. Y.; Yen, C. Y.; Chung, Y. C. Biodegradation of Crystal Violet by Pseudomonas Putida. *Biotechnol. Lett.* **2007**, *29*, 391−396.
(13) Wang, J. L.; Xu, L. J. Advanced Oxidation Processes for Wastewater Treatment: Formation of Hydroxyl Radical and Application. *Crit. Rev. Environ. Sci. Technol.* **2012**, *42*, 251−325.
(14) Yin, S. F.; Xu, B. Q.; Ng, C. F.; Au, C. T. Nano Ru/CNTs: A Highly Active and Stable Catalyst for The Generation of CO_x-Free Hydrogen in Ammonia Decomposition. *Appl. Catal., B* **2004**, *48*, 237−241.
(15) Rhadfi, T.; Piquemal, J. Y.; Sicard, L.; Herbst, F.; Briot, E.; Benedetti, M.; Atlamsani, A. Polyol-Made Mn_3O_4 Nanocrystals as Efficient Fenton-Like Catalysts. *Appl. Catal., A* **2010**, *386*, 132−139.
(16) Neyens, E.; Baeyens, J. A Review of Classic Fenton's Peroxidation as an Advanced Oxidation Technique. *J. Hazard. Mater.* **2003**, *98*, 33−50.
(17) Parra, S.; Guasaquillo, I.; Enea, O.; Mielczarski, E.; Mielczarki, J.; Albers, P.; Kiwi-Minsker, L.; Kiwi, J. Abatement of An Azo Dye on Structured C-Nafion/Fe-Ion Surfaces by Photo-Fenton Reactions Leading to Carboxylate Intermediates With A Remarkable Biodegradability Increase of The Treated Solution. *J. Phys. Chem. B* **2003**, *107*, 7026−7035.
(18) Gregor, C.; Hermanek, M.; Jancik, D.; Pechousek, J.; Filip, J.; Hrbac, J.; Zboril, R. The Effect of Surface Area and Crystal Structure on The Catalytic Efficiency of Iron(iii) Oxide Nanoparticles in Hydrogen Peroxide Decomposition. *Eur. J. Inorg. Chem.* **2010**, 2343−2351.
(19) Lim, H.; Lee, J.; Jin, S.; Kim, J.; Yoon, J.; Hyeon, T. Highly Active Heterogeneous Fenton Catalyst Using Iron Oxide Nanoparticles Immobilized in Alumina Coated Mesoporous Silica. *Chem. Commun.* **2006**, 463−465.
(20) Hermanek, M.; Zboril, R.; Medrik, N.; Pechousek, J.; Gregor, C. Catalytic Efficiency of Iron(iii) Oxides in Decomposition of Hydrogen Peroxide: Competition Between The Surface Area and Crystallinity of Nanoparticles. *J. Am. Chem. Soc.* **2007**, *129*, 10929−10936.
(21) Gao, L. Z.; Zhuang, J.; Nie, L.; Zhang, J. B.; Zhang, Y.; Gu, N.; Wang, T. H.; Feng, J.; Yang, D. L.; Perrrett, S.; Yan, X. Y. Intrinsic Peroxidase-Like Activity of Ferromagnetic Nanoparticles. *Nat. Nanotechnol.* **2007**, *2*, 577−583.
(22) Pham, A. L. T.; Lee, C.; Doyle, F. M.; Sedlak, D. L. A Silica-Supported Iron Oxide Catalyst Capable of Activating Hydrogen Peroxide at Neutral pH Values. *Environ. Sci. Technol.* **2009**, *43*, 8930−8935.
(23) Iurascu, B.; Siminiceanu, I.; Vione, D.; Vicente, M. A.; Gil, A. Phenol Degradation in Water Through A Heterogeneous Photo-Fenton Process Catalyzed by Fe-Treated Laponite. *Water Res.* **2009**, *43*, 1313−1322.
(24) Chen, Q. Q.; Wu, P. X.; Li, Y. Y.; Zhu, N. W.; Dang, Z. Heterogeneous Photo-Fenton Photodegradation of Reactive Brilliant Orange X-GN Over Iron-Pillared Montmorillonite Under Visible Irradiation. *J. Hazard. Mater.* **2009**, *168*, 901−908.
(25) Duarte, F.; Maldonado-Hodar, F. J.; Perez-Cadenas, A. F.; Madeira, L. M. Fenton-Like Degradation of Azo-Dye Orange II Catalyzed by Transition Metals on Carbon Aerogels. *Appl. Catal., B* **2009**, *85*, 139−147.
(26) Ramirez, J. H.; Maldonado-Hodar, F. J.; Perez-Cadenas, A. F.; Moreno-Castilla, C.; Costa, C. A.; Madeira, L. M. Azo-Dye Orange II Degradation by Heterogeneous Fenton-Like Reaction Using Carbon-Fe Catalysts. *Appl. Catal., B* **2007**, *75*, 312−323.
(27) Kasiri, M. B.; Aleboyeh, H.; Aleboyeh, A. Degradation of Acid Blue 74 Using Fe-ZSM5 Zeolite as A Heterogeneous Photo-Fenton Catalyst. *Appl. Catal., B* **2008**, *84*, 9−15.
(28) Qiu, Z. M.; He, Y. B.; Liu, X. C.; Yu, S. X. Catalytic Oxidation of the Dye Wastewater With Hydrogen Peroxide. *Chem. Eng. Process.* **2005**, *44*, 1013−1017.
(29) Timofeeva, M. N.; Jhung, S. H.; Hwang, Y. K.; Kim, D. K.; Panchenko, V. N.; MeIgunov, M. S.; Chesalov, Y. A.; Chang, J. S. Ce-Silica Mesoporous SBA-15-Type Materials for Oxidative Catalysis: Synthesis, Characterization, and Catalytic Application. *Appl. Catal., A* **2007**, *317*, 1−10.
(30) Zhan, W. C.; Guo, Y. L.; Wang, Y. Q.; Liu, X. H.; Guo, Y.; Wang, Y. S.; Zhang, Z. G.; Lu, G. Z. Synthesis of Lanthanum-Doped MCM-48 Molecular Sieves and Its Catalytic Performance for The Oxidation of Styrene. *J. Phys. Chem. B* **2007**, *111*, 12103−12110.
(31) Gao, T.; Norby, P.; Krumeich, F.; Okamoto, H.; Nesper, R.; Fjellvag, H. Synthesis and Properties of Layered-Structured Mn_5O_8 Nanorods. *J. Phys. Chem. C* **2010**, *114*, 922−928.
(32) Bai, Z. C.; Sun, B.; Fan, N.; Ju, Z. C.; Li, M. H.; Xu, L. Q.; Qian, Y. T. Branched Mesoporous Mn_3O_4 Nanorods: Facile Synthesis and Catalysis in The Degradation of Methylene Blue. *Chem.- Eur. J.* **2012**, *18*, 5319−5324.
(33) Fei, J. B.; Cui, Y.; Yan, X. H.; Qi, W.; Yang, Y.; Wang, K. W.; He, Q.; Li, J. B. Controlled Preparation of MnO_2 Hierarchical Hollow Nanostructures and TheirApplication in Water Treatment. *Adv. Mater.* **2008**, *20*, 452−456.
(34) Chen, Y. C.; Duan, Z. Y.; Min, Y. L.; Shao, M. W.; Zhao, Y. G. Synthesis, Characterization and Catalytic Property of Manganese Dioxide With Different Dtructures. *J. Mater. Sci.: Mater. Electron.* **2011**, *22*, 1162−1167.
(35) Sui, N.; Duan, Y. Z.; Jiao, X. L.; Chen, D. R. Large-Scale Preparation and Catalytic Properties of One-Dimensional Alpha/Beta-MnO_2 nanostructures. *J. Phys. Chem. C* **2009**, *113*, 8560−8565.
(36) Wu, C. H.; Chang, C. L. Decolorization of Reactive Red 2 by Advanced Oxidation Processes: Comparative Studies of Homogeneous and Heterogeneous Systems. *J. Hazard. Mater.* **2006**, *128*, 265−272.
(37) Lu, A. H.; Schuth, F. Nanocasting: A Versatile Strategy for Creating Nanostructured Porous Materials. *Adv. Mater.* **2006**, *18*, 1793−1805.

(38) Zhu, S. M.; Zhou, Z. Y.; Zhang, D.; Wang, H. H. Synthesis of Mesoporous Amorphous MnO_2 From SBA-15 Via Surface Modification and Ultrasonic Waves. *Microporous Mesoporous Mater.* **2006**, *95*, 257−264.
(39) Tian, Z. R.; Tong, W.; Wang, J. Y.; Duan, N. G.; Krishnan, V. V.; Suib, S. L. Manganese Oxide Mesoporous Structures: Mixed-Valent Semiconducting Catalysts. *Science* **1997**, *276*, 926−930.
(40) Jiao, F.; Harrison, A.; Hill, A. H.; Bruce, P. G. Mesoporous Mn_2O_3 and Mn_3O_4 With Crystalline Walls. *Adv. Mater.* **2007**, *19*, 4063−4066.
(41) Toberer, E. S.; Schladt, T. D.; Seshadri, R. Macroporous Manganese Oxides With Regenerative Mesopores. *J. Am. Chem. Soc.* **2006**, *128*, 1462−1463.
(42) Kim, J. M.; Huh, Y. S.; Han, Y. K.; Cho, M. S.; Kim, H. J. Facile Synthesis Route to Highly Crystalline Mesoporous Gamma-MnO_2 nanospheres. *Electrochem. Commun.* **2012**, *14*, 32−35.
(43) Zhang, Y. G.; Chen, L. Y.; Zheng, Z.; Yang, F. L. A Redox-Hydrothermal Route to Beta-MnO_2 Hollow Octahedra. *Solid State Sci.* **2009**, *11*, 1265−1269.
(44) Yuan, C. Z.; Hou, L. R.; Yang, L.; Li, D. K.; Shen, L. F.; Zhang, F.; Zhang, X. G. Facile Interfacial Synthesis of Flower-Like Hierarchical α-MnO_2 Sub-Microspherical Superstructures Constructed by Two-Dimension Mesoporous Nanosheets and Their Application in Electrochemical Capacitors. *J. Mater. Chem.* **2011**, *21*, 16035−16041.
(45) Liu, M.; Zhang, G. J.; Shen, Z. R.; Sun, P. C.; Ding, D. T.; Chen, T. H. Synthesis and Characterization of Hierarchically Structured Mesoporous MnO_2 and Mn_2O_3. *Solid State Sci.* **2009**, *11*, 118−128.
(46) Whang, D.; Jin, S.; Wu, Y.; Lieber, C. M. Large-Scale Hierarchical Organization of Nanowire Arrays for Integrated Nanosystems. *Nano Lett.* **2003**, *3*, 1255−1259.
(47) Park, S.; Lim, J. H.; Chung, S. W.; Mirkin, C. A. Self-Assembly of Mesoscopic Metal-Polymer Amphiphiles. *Science* **2004**, *303*, 348−351.
(48) Ai, L. H.; Yue, H. T.; Jiang, J. Sacrificial Template-Directed Synthesis of Mesoporous Manganese Oxide Architectures With Superior Performance for Organic Dye Adsorption. *Nanoscale* **2012**, *4*, 5401−5408.
(49) Du, Y. C.; Meng, Q.; Wang, J. S.; Yan, J.; Fan, H. G.; Liu, Y. X.; Dai, H. X. Three-Dimensional Mesoporous Manganese Oxides and Cobalt Oxides: High-Efficiency Catalysts for The Removal of Toluene and Carbon Monoxide. *Microporous Mesoporous Mater.* **2012**, *162*, 199−206.
(50) Xu, M. W.; Jia, W.; Bao, S. J.; Su, Z.; Dong, B. Novel Mesoporous MnO_2 for High-Rate Electrochemical Capacitive Energy Storage. *Electrochim. Acta* **2010**, *55*, 5117−5122.
(51) Li, J. F.; Xi, B. J.; Zhu, Y. C.; Li, Q. W.; Yan, Y.; Qian, Y. T. A Precursor Route to Synthesize Mesoporous Gamma-MnO_2 Microcrystals and Their Applications in Lithium Battery and Water Treatment. *J. Alloys Compd.* **2011**, *509*, 9542−9548.
(52) Yuan, C. Z.; Gao, B.; Su, L. H.; Zhang, X. G. Interface Synthesis of Mesoporous MnO_2 and Its Electrochemical Capacitive Behaviors. *J. Colloid Interface Sci.* **2008**, *322*, 545−550.
(53) Lin, Y.; Skaff, H.; Emrick, T.; Dinsmore, A. D.; Russell, T. P. Nanoparticle Assembly and Transport at Liquid-Liquid Interfaces. *Science* **2003**, *299*, 226−229.
(54) Yang, X. H.; Wang, Y. G.; Xiong, H. M.; Xia, Y. Y. Interfacial Synthesis of Porous MnO_2 and Its application in Electrochemical Capacitor. *Electrochim. Acta* **2007**, *53*, 752−757.
(55) Yang, Z. H.; Zhang, Y. C.; Zhang, W. X.; Wang, X.; Qian, Y. T.; Wen, X. G.; Yang, S. H. Nanorods of Manganese Oxides: Synthesis, Characterization and Catalytic Application. *J. Solid State Chem.* **2006**, *179*, 679−684.